Chromosome disentanglement driven via optimal compaction of loop-extruded brush structures

Sumitabha Brahmachari[a,b,1] and John F. Marko[a,c]

[a]Department of Physics and Astronomy, Northwestern University, Evanston, IL 60208; [b]Center for Theoretical Biological Physics, Rice University, Houston, TX 77005; and [c]Department of Molecular Biosciences, Northwestern University, Evanston, IL 60208

Edited by Leonid A. Mirny, Massachusetts Institute of Technology, Cambridge, MA, and accepted by Editorial Board Member Kiyoshi Mizuuchi October 23, 2019 (received for review April 29, 2019)

Eukaryote cell division features a chromosome compaction–decompaction cycle that is synchronized with their physical and topological segregation. It has been proposed that lengthwise compaction of chromatin into mitotic chromosomes via loop extrusion underlies the compaction-segregation/resolution process. We analyze this disentanglement scheme via considering the chromosome to be a succession of DNA/chromatin loops—a polymer "brush"—where active extrusion of loops controls the brush structure. Given type-II DNA topoisomerase (Topo II)-catalyzed topology fluctuations, we find that interchromosome entanglements are minimized for a certain "optimal" loop that scales with the chromosome size. The optimal loop organization is in accord with experimental data across species, suggesting an important structural role of genomic loops in maintaining a less entangled genome. Application of the model to the interphase genome indicates that active loop extrusion can maintain a level of chromosome compaction with suppressed entanglements; the transition to the metaphase state requires higher lengthwise compaction and drives complete topological segregation. Optimized genomic loops may provide a means for evolutionary propagation of gene-expression patterns while simultaneously maintaining a disentangled genome. We also find that compact metaphase chromosomes have a densely packed core along their cylindrical axes that explains their observed mechanical stiffness. Our model connects chromosome structural reorganization to topological resolution through the cell cycle and highlights a mechanism of directing Topo II-mediated strand passage via loop extrusion-driven lengthwise compaction.

genome organization | chromosome topology | loop extrusion | lengthwise compaction | cylindrical polymer brush

Chromosomes are biopolymer structures made up of long, multimegabase-pair DNAs bound by proteins, residing in confined spaces. For eukaryotes, the nucleus is the confining compartment, while bacterial chromosomes are confined by the cell itself. Without their organization into looped structures, the confinement would lead to cellular chromosomes forming an entangled, semidilute polymer solution (1); i.e., the fraction of the total confinement volume occupied by all of the genomic segments (average volume fraction) is high enough to force strong overlap between different chromosomes (simply considered as linear polymers). However, as we argue in the following, the organization of chromosomes into loops with a "polymer-brush"–like architecture (Fig. 1*B*) leads to lower interchromosomal overlap for a fixed volume fraction.

An important question in chromosome biophysics is, How can topology-manipulating enzymes, type-II DNA topoisomerases (Topo II) that catalyze the passage of one genomic segment through another, drive global disentanglement of chromosomes? Since individual Topo IIs cannot sense the global entanglement topology of chromosomes, we consider Topo II to facilitate random strand passage. This lets the chromosomes pass through each other akin to a "phantom" polymer chain where the interchromosomal topology fluctuates (2). However, random strand passage is not enough to completely disentangle long linear polymers, because the entropically favored state is the one with higher interchromosomal mixing or volume overlap. Modeling chromosomes as arrays of polymer loops, we find that the compaction generated from chromosomal loop organization is capable of driving interchromosome disentanglement and segregation, under the conditions of fluctuating topology. Our results are complementary to and to some extent establish a theoretical description of recent simulation results that show how loop-extruding protein machines are able to geometrically and topologically organize long polymer-like chromosomes (3–5).

Eukaryote chromosomes undergo significant and highly ordered compaction during mitosis. This process cannot be "condensation" in the usual sense of that term: Uncontrolled self-adhesion of chromatin will lead to a compact and highly entangled genomic globule. More plausibly, chromosome segregation is based on "lengthwise compaction" simultaneous with Topo II-mediated topology changes, cooperating to drive progressive physical and topological segregation (6, 7). Processive extrusion of genomic loops by loop-extruding enzymes has been proposed to underlie lengthwise compaction (3, 8) and the formation of the long-observed cylindrical brush (loop array) structure of metaphase chromosomes (9–11). The "loop-extrusion" hypothesis proposes a microscopic mechanism to achieve lengthwise compaction of chromosomes based on molecular-motor–generated tension along the polymer contour

Significance

Topology simplification of chromosomes occurs simultaneously with their segregation during cell division and is driven by interplay between chromosome compaction and topology fluctuations. Loop extrusion, a mechanism of genome organization where DNA/chromatin loops are actively extruded to form a cylindrical polymer "brush," has been proposed as a mechanism underlying chromosome folding and compaction. In this study, we show that such a brush model possesses an optimal loop size that simultaneously maximizes lengthwise compaction and minimizes interchromosomal entanglement. Our model predicts the optimal loop size and other experimentally observable properties of chromosomes for a wide range of organisms of varied genome size.

Author contributions: J.F.M. designed research; S.B. performed research; and S.B. and J.F.M. wrote the paper.

The authors declare no competing interest.

This article is a PNAS Direct Submission. L.A.M. is a guest editor invited by the Editorial Board.

[1]To whom correspondence may be addressed. Email: sumitabha@u.northwestern.edu.

This article contains supporting information online at https://www.pnas.org/lookup/suppl/doi:10.1073/pnas.1906355116/-/DCSupplemental.

First published November 22, 2019.

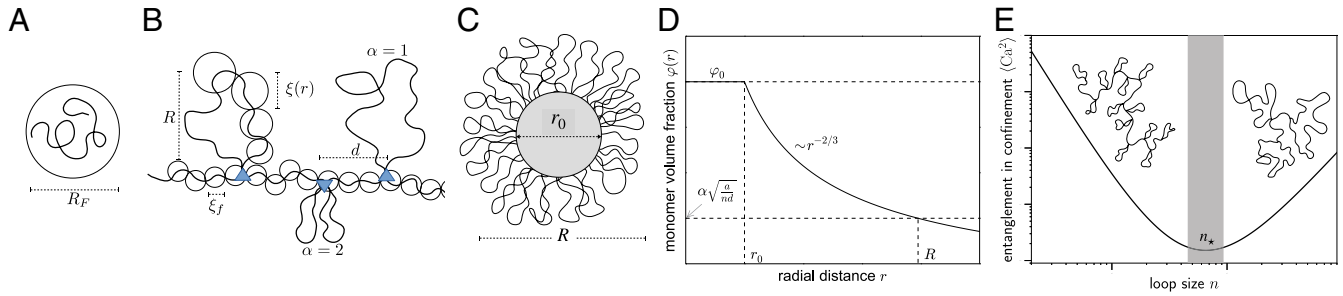

Fig. 1. (*A*) Flory radius or equilibrium dimension of a self-avoiding polymer (Eq. **1**). (*B*) Sketch of loop-extruded chromosome showing chromatin loops connected by a backbone, where circles represent blobs of size ξ that depend on the radial distance from the backbone. Of the 3 schematic loops sketched, the middle one is divalent ($\alpha = 2$) and the other 2 are monovalent ($\alpha = 1$). (*C*) Cross-sectional view of compacted chromosome. Circular cross-section corresponding to the gray-shaded area is the densely packed chromatin core of width r_0. (*D*) Monomer volume fraction $\varphi(r)$ is maximum inside the core [$\varphi_0 \approx 1$] and decays radially outward. (*E*) For a fixed genome size *N*, backbone size *m*, and nuclear volume, interchromosome entanglements per chromosome $\langle Ca^2 \rangle$ (Eq. **4**) show a minimum for an optimal configuration with loop size $n_\star$ (shown by a shaded region). This follows from the geometry and finite size of chromosomes. Schematic pictures of finite-size chromosomes in the small- and large-loop regimes are shown.

(3, 8). In other models of chromosome compaction, such a compaction-generating tension may be effectively generated by mechanisms like supercoiling flux arising from transcription and replication (12), or "sliding" of genomic contacts driven by directed motion of molecular slip links (13, 14), or diffusion of genomic segments in a hypothesized data-driven potential (15, 16).

Structural maintenance of chromosomes (SMC) complexes are thought to be responsible for organizing chromosome structure (17–25) and recently have been directly observed to processively translocate and loop extrude DNA (26, 27). The 3D conformation of the interphase genome has been observed to be organized into loops that are associated with regulation of gene expression, and these loops appear to be actively driven by a concerted action of proteins like SMC complexes and other architectural proteins (20, 24, 25, 28–33). Electron microscope images of metaphase chromosomes have directly observed the loop organization, supporting a polymer brush model with radially emanating loops (9, 10, 34).

We model chromosomal DNA/chromatin as a long polymer and chromosomes as a polymer brush-like steady-state structure where the "bristles" represent chromatin loops. Comparing with experimentally observed genomic loops, we find that chromosomes appear to be organized into "optimal"-sized loops that maximize compaction and simultaneously minimize interchromosome entanglement. Qualitatively, the optimal size occurs since for small loops, chromosomes have a long axial length and easily become highly entangled with other chromosomes. As the loops grow in size, the chromosome is gradually lengthwise compacted to become a cylindrical brush of size smaller than the original chromosome (Eq. **2**), and entanglements between chromosomes are reduced. If the loops become so large that they are comparable to the size of the chromosomes themselves, the chromosome becomes a "star polymer" with long bristles which once again become highly entangled with bristles of neighboring chromosomes (Fig. 1*D*). While we discuss our results primarily in the context of eukaryotes, we also show how they can be applied to bacterial chromosomes.

Here, we show that loop-extruding motors, capable of exerting forces in the piconewton range, are sufficient to drive compaction to a stage where osmotic repulsion between chromosomes will lead to disentangled chromosomes, given that entanglement topology is allowed to change (Topo II is active). Compaction tension generates stress in chromosomes, which is then relaxed through entanglement release by Topo II: The coupling of compaction to topological simplification provides the key driving force directing Topo II to disentangle the genome.

Polymer Model and Methods

We consider chromatin (or DNA coated with proteins) as a long self-avoiding polymer that is organized as an array of loops that resembles a "bottle brush" polymer. The brush is in a constrained local thermal equilibrium, because maintaining the brush structure requires continual work to be done by SMC complexes that secure the loop anchors against thermal agitation. The motor activity of SMC complexes leads to active reorganization of the chromosome polymer, but since the self-organization time is much longer than the equilibration (Rouse) time of a typical loop even including entanglement release dynamics by Topo II (*Discussion*), we may employ static polymer scaling laws.

We implement a 2-level polymer physics model: At shorter length scales chromatin behaves as a self-avoiding polymer; then, at longer lengths—comparable to chromosome radii, where interchromosomal interactions dominate—we consider chromosomes as effective polymers made up of cylindrical brush segments. Our chromatin is a chain of spherical monomers of diameter a, such that a chromatin chain of N monomers "swells" up due to self-avoiding monomer correlations and assumes a dimension given by its "Flory radius":

$$R_F(N) = aN^{3/5}. \quad [1]$$

We make the choice of monomer as one nucleosome (200 bp DNA): $a = 10$ nm. Recent electron-microscopy (35–37) and superresolution imaging analyses (38) are in line with a highly flexible chromatin fiber model with each nucleosome as a polymer segment, rather than a more traditional "stiff 30-nm fiber" model. In the bacterial case, the polymer is DNA coated by nucleoid-associated proteins with a similar value of a but containing 150 bp DNA. The cylindrical aspect ratio of the bacterial "chromatin" monomer is not critical to our results (*SI Appendix*).

When multiple chromatin chains (say, k chains, such that the genome size is $\mathcal{G} = Nk$) are confined within a volume $V \ll kR_F(N)^3$, the semidilute regime, self-avoiding interactions are screened at lengths larger than the correlation length or "blob" size $\xi = a\phi^{-3/4}$ that is set by the monomer volume fraction $\phi = kNa^3/V$ (1). This scaling remains valid until the monomers fill the entire space, $\phi \approx 1$, the melt regime. The average volume fraction of the confined genome is in the semidilute regime (*SI Appendix*, Table S1), where the blob size is typically in the hundreds-of-nanometers range.

The chromatin blob size inside the brush, however, is smaller than the confinement-induced limit, because of the higher volume fraction driven by compaction. Loop extrusion-generated tension, f (in the piconewton range) establishes a smaller blob

size, $\sim k_B T/f$ (tens-of-nanometers range; recall that $k_B T \approx 4$ pN·nm), and drives a transition to a compact state where the local environment approaches the melt regime. Note that this transition is fundamentally different from that arising under "bad solvent" conditions, i.e., where instead of self-avoidance, intermonomer contact is energetically favored. Unlike bad solvents, loop extrusion, due to its topological nature, drives only the monomers within a chromosome toward a melt. Loop extrusion acts against chromatin self-avoidance and entropic mixing to preferentially demix chromatin associated with different chromosomes and thus acts as an effective thermodynamic force driving segregation or individualization of chromosomes. This gives rise to an effective chromosome polymer that is made up of brush segments. In the following we analyze a homogeneous cylindrical brush and use blobs made up of this shorter and stiffer brush polymer to compute nearby contacts between interchromosomal segments as a measure of entanglement (7).

An important assumption in the abovementioned effective-polymer renormalization is that of topology fluctuations; i.e., Topo II facilitates random strand passage. We treat chromatin as self-avoiding with the caveat that at long timescales corresponding to large structural reorganization of chromosomes, the effective polymers behave as phantom chains (2). This means at short timescales of equilibration of blobs, there are topological constraints; however, when a certain constraint persists over timescales relevant to Topo dynamics ($\sim$1 strand passage per second), it is released with a ± 1 linking number change. The relevant measure of genome entanglement in a transition from interphase to mitosis is the interchromosome linking number change. We find that under topology fluctuations, the distribution of interchromosome linking number is effectively controlled by lengthwise compaction. Lower compaction in interphase exhibits a wider distribution, which becomes narrower under a higher level of lengthwise compaction, driving Topo II-mediated unlinking or decatenation.

Cylindrical Polymer Brush Chromosomes. We model chromosomes as a succession of chromatin loops connected by a chromatin backbone (Fig. 1*B*). The resulting cylindrical bottlebrush polymer is characterized by 3 independent structural parameters: loop size n, the average number of nucleosome monomers per loop; backbone size m, the average number of nucleosome monomers between adjacent loop anchors; and loop valency α, the degree of subdivision (branching) of larger loops into smaller ones. A loop of size n with a valency α indicates there are α subloops each of size n/α associated with the same anchoring location (Fig. 1*B*).

When the backbone is comparable to the loops ($n \lesssim m$), adjacent loops overlap only weakly, and the brush approaches the "random coil" limit (Eq. **1**). This corresponds to the average semidilute solution, where the monomer densities inside and outside a chromosome are similar. Alternately, when $m \ll n$, adjacent loops strongly overlap and the resulting structure resembling a polymer brush is significantly more compact, in addition to being stiffer.

A key parameter for the brush is the interloop distance d, the spatial distance between adjacent loop anchors: d is the steady-state end-to-end extension of the backbone segment of m monomers. A polymer brush morphology of overlapping adjacent loop bristles requires $d < R_F(n)$ and $d > R_F(m)$. For a fixed m and n, the value of d is set by a balance between the osmotic repulsion among adjacent loops that drives an increase in d ($f \approx k_B T a^{5/8} n^{3/8} d^{-13/8}$) and the elastic restoring force of the backbone polymer which favors a decrease in d ($f \approx k_B T a^{-5/2} m^{-3/2} d^{3/2}$) (*SI Appendix*). This force balance furnishes $d = a n^{3/25} m^{12/25}$ that is valid until the stretching force reaches a critical value, $f_\star = k_B T/a \approx 0.4$ pN, corresponding to a completely stretched backbone ($d \sim ma$). This transition occurs when the backbone size is a small fraction of the loop size, $m_\star = n^{3/13}$ (39).

As is typical for a cylindrical polymer brush, the monomer volume fraction decreases radially outward, causing an osmotic pressure gradient that radially stretches the loops and establishes a long thermal bending persistence length reflecting a stiffening response for a brush with closely spaced loops (*SI Appendix*) (34, 39–41).

The average monomer volume fraction inside the brush is higher for lower interloop distance and higher loop branching: $\varphi \sim \alpha^{2/3} d^{-2/3}$. This generates a region along the backbone of the brush, which we refer to as the "core" that features dense packing of the monomers ($\varphi_{core} \approx 1$) and a high osmotic pressure $\sim k_B T/a^3$ (Fig. 1 *C* and *D*). The width of the core is proportional to the loop valency and inversely proportional to the interloop distance: $r_0 \approx \alpha a^2/d$ (*SI Appendix*). This relation, derived from the geometric condition that the surface of the core forms a surface saturated by "grafted" loops, indicates that more closely packed loops and loops with higher branching generate a thicker core. We note that while the existence of a maximal-density core has been long discussed in connection with spherical polymer "micelles" (42), the cylindrical polymer brush literature has not recognized this possibility, which appears to be key to understanding chromosome folding.

Brush Chromosomes as an Effective Polymer. We consider the brush chromosomes as a thicker and shorter "noodle"-like polymer constituted of the underlying chromatin. The renormalized brush contour length L' is shorter than the chromatin contour $L = Na$. The renormalized thickness R is larger than chromatin thickness a and shows a monotonic increase with loop size. However, L' is nonmonotonic with loop size n:

$$L' \approx Nd/n + R_F(n). \quad [2]$$

The first term corresponds to the cylindrical part of the brush where there are N/n loops, each contributing $d \sim n^{3/25} m^{12/25}$ to the axial length L'—constituting a net contribution that decreases with the loop size. The second term is from the loops at the ends of the cylinder that are less confined than their counterparts in the middle of the brush. These hemispherical ends of the chromosome have radii on the order of the chromosome thickness and contain a large amount of chromatin (e.g., megabases for larger human chromosomes) and are typically much larger than telomeres. As the average loop size increases, the contribution of the "end loops" to the axial length increases until one has a "star" polymer which is all ends and no axis, with size of a Flory polymer of n monomers (Eq. **1**). We note that Eq. **2** corresponds to the brush limit of the chromosomes where $n \gg m$ or $n + m \approx n$.

Minimization of the renormalized contour length gives an optimal loop size

$$n_\star = m^{12/37} N^{25/37} \quad [3]$$

that maximizes compaction. A renormalized chromosome with loops larger than the optimal size begins to resemble a star polymer or a micelle, whereas loops smaller than the optimal size make the structure a thin brush with a long axial length. Both of these nonoptimal possibilities are less compact than the optimal loop brush.

Entanglement between Chromosomes in a Confined Volume. We quantify entanglement between chromosomes using their mean-squared interchromosome linking (catenation) number $\langle \mathrm{Ca}^2 \rangle$, which measures the width of the catenation number distribution. $\langle \mathrm{Ca}^2 \rangle$ is readily computed from the number of near (polymer segment-scale) encounters between the brush chromosomes (6)

(the "catenation number" Ca is used in the DNA topology field to denote the Gaussian linking number of distinct duplex DNA molecules). Given freely fluctuating topology, each close encounter between chromosomes contributes $\sim\pm1$ to the inter-chromosome linking number. Since Topo II is a locally acting enzyme that cannot sense the global linking between any 2 chromosomes, the only means by which chromosomes may disentangle in the presence of Topo II-mediated strand-passage activity is via elimination of interchromosomal contacts, which may be achieved by driving higher compaction.

The number of close encounters or collisions between chromosome segments that determines the level of entanglement scales linearly with the number of polymer segments: $\mathcal{N}_{\rm coll}\approx N\phi^{5/4}$ (6) (*SI Appendix*). As previously shown in ref. 6, the contribution of this blob-collision number to interchromosomal topology is obtained using $\langle {\rm Ca}^2\rangle_0\approx\mathcal{N}_{\rm coll}/n_c$, where the proportionality constant $n_c\approx100$ [determined numerically (6, 43)] is the number of contacts required to have a ±1 contribution to catenation [n_c is a scale similar to the "entanglement length" familiar from polymer physics (1)].

The number of collisions between segments of the effective brush polymer, $\mathcal{N}'_{\rm coll}$, is much lower than that for chromatin $\mathcal{N}_{\rm coll}$ due to the smaller number of statistical segments of a polymer brush, $N'\approx L'/R\ll N$. This leads to an interchromosomal entanglement level for the brush state ($\langle {\rm Ca}^2\rangle$) that can be controlled via the compaction state of the chromosomes and is significantly lower than that for unfolded chromatin ($\langle {\rm Ca}^2\rangle_0$),

$$\frac{\langle {\rm Ca}^2\rangle}{\langle {\rm Ca}^2\rangle_0}\approx\left(\frac{R_F(N')}{R_F(N)}\right)^{15/4}=\left(\frac{L'}{R_F(N)}\right)^{15/4}=\left(\frac{m}{N}\right)^{27/37}, \quad [4]$$

where the last 2 equalities follow for optimal brushes ($N'\sim1$). Since $m\ll N$, there is a strong suppression of the entanglement level in a solution of optimal brushes, compared to a semidilute solution of linear chromatin chains (for calculation details see *SI Appendix*).

We have used a flexible self-avoiding polymer approach for describing chromatin (with nucleosome-scale monomers); we also employ this description for bacterial "chromatin" (DNA covered by nucleoid-associated proteins [NAPs]), as well as for the conformational statistics of the "brush" polymers formed by loop extrusion. In the bacterial chromatin and brush-polymer analysis, we note that for situations where the polymer segments are much longer than their width, the weak excluded volume between monomers might oblige one to follow the approach of ref. 44, which considers the situation of long, thin polymer segments. For this limit, one has a concentration range in which excluded volume is too weak at short distances to generate self-avoiding-walk statistics and where one should use marginal or "theta" solvent conditions. For the situations considered in this paper, we have found that effects of segment shape are not critical to the results, so we follow the simpler self-avoiding polymer formulation; discussion of segment-aspect-ratio effects can be found in *SI Appendix*.

Results

Optimal Loops Maintain a Basal Level of Chromosome Compaction and Suppress Interchromosomal Entanglements. Optimal loop size minimizes chromosome axial length L' (Eq. **2**). The existence of the optimal state arises from the fact that when the loops are small, there are a large number of them, each contributing about one interloop distance d to L'. On the other hand, if the loops become so large that the equilibrium unperturbed size of the loops at the end of the cylindrical brush begins to dominate, L' is again large. A loop size between these limits minimizes L'. Fig. 2 shows the optimal subloop size, which is obtained by dividing the optimal size by the valency or the number of loop branches.

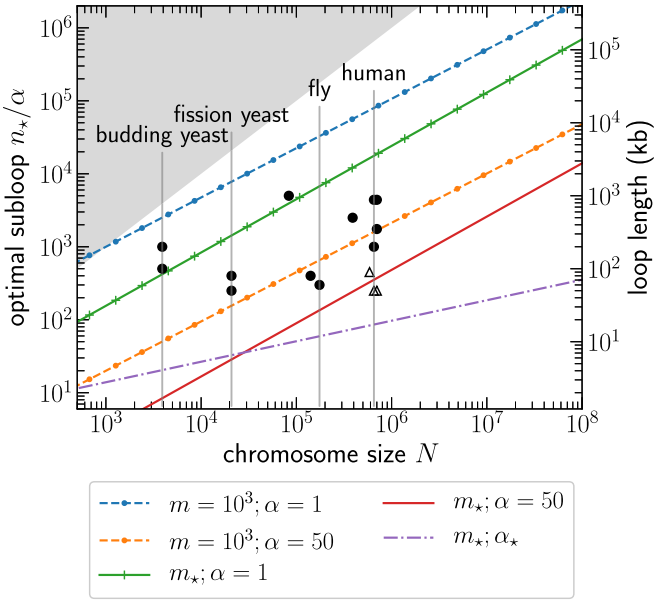

Fig. 2. Optimal loops of size $n_\star$ minimize axial length of the brush chromosome and suppress chromosomal entanglements. Loop size divided by valency α (number of branches) gives the size of subloops, plotted versus the total number of chromosomal units *N*. Curves correspond to different numbers of monomers in the backbone segment between 2 consecutive loops *m* and valency α. Optimal loops are larger for larger *m*. A fully stretched backbone, owing to the tension generated from overlapping adjacent loops, corresponds to $m=m_\star$ (Table 1), the minimum size of the backbone for an optimal loop. Higher valency α leads to smaller subloops due to increased loop branching and increases the density of the monomers in the interior of the brush. Valency $\alpha_\star$ scales with *N* and corresponds to a phenomenological value for metaphase chromosomes (Table 1). The gray-shaded region is inaccessible, as it corresponds to a loop size greater than the chromosome length. Solid circles are experimental data for "loop domains" in the interphase genome obtained from chromosome contact or Hi-C maps (28–30, 32, 33); open triangles denote loops identified from electron-microscope images of metaphase chromosomes (9, 10). The data indicate that an entanglement-suppressing optimal loop size is maintained throughout the cell cycle: During interphase, the loops have a lower valency and are less compact, whereas during mitosis, the loops are heavily branched, leading to smaller subloops. The experimental data also respect the physical limits imposed by our tandem-loop model. The *y* axis on the right shows the loop lengths in kilobase pair units.

In terms of interloop-anchor "backbone" segment size m, optimal loops are larger for a brush with larger m (Fig. 2). To attain the same brush axial length and stretching tension along the backbone, a configuration with longer backbone segments requires larger loops. Increasing m eventually leads to nonoverlapping adjacent loops, the case for a random-coil polymer. Making the backbone small leads to the limiting size $m_\star$, where the tension from overlap of closely anchored loops completely stretches the backbone ($d\sim m_\star\sim N^{15/89}$) (Table 1). The optimal brush with a fully stretched backbone has the minimum axial length L', associated with an axial stretching tension $f_\star=k_BT/a\approx0.4$ pN. Compaction with subpiconewton stretching forces is not likely to disrupt the nucleosomes or the integrity of the chromatin fiber, an important physical constraint on genome folding.

The different lines in Fig. 2 correspond to values of m and α that represent different overall conformations of brush chromosomes. The blue dashed line ($m=10^3$ and $\alpha=1$) corresponds to a "sparsely grafted" configuration of monovalent loops, featuring minimal overlap between adjacent loops. While the orange dashed line ($m=10^3$ and $\alpha=50$) corresponds to a sparse

Table 1. Example values of the minimum backbone size $m_\star = N^{15/89}$ and metaphase valency $\alpha_\star = (0.5)N^{40/89}$

Organism	Chromosome size, N	Minimum backbone size, $m_\star$	Metaphase valency, $\alpha_\star$
Budding yeast	4×10^3	5	20
Human	6.5×10^5	10	200
Newt	2×10^7	20	1,000

configuration of branched loops. The green solid line ($m = m_\star$ and $\alpha = 1$) corresponds to a "dense" regime of brush where adjacent monovalent loops are closely grafted, forcing strong interloop repulsion and a stiff response to bending. The red solid line ($m = m_\star$ and $\alpha = 50$) is for a dense brush with a higher degree of loop branching. Finally, the purple dotted-dashed line ($m = m_\star$ and $\alpha = \alpha_\star$) corresponds to a dense, stiff brush with highly branched loops—a model for compact metaphase chromosomes; the degree of branching $\alpha_\star$, which scales with N (see below and Table 1), is determined from the elastic modulus of metaphase chromosomes (45).

Chromosome conformation capture experiments (e.g., Hi-C) studying the ensemble-average conformation of the interphase genome of various species find a characteristic loop size (29, 31–33) (Fig. 2, solid circles). Fig. 2 suggests that these interphase chromosome loops maintain a brush-like structure of the chromosome, driving a level of compaction quantitatively similar to optimal loops. Loop sizes obtained from electron-microscope images of metaphase chromosomes (9, 10) are somewhat smaller than those of interphase loops (Fig. 2, open triangles). Increasing interphase loop valency is a conceivable way to drive mitotic chromosome compaction, but Hi-C experiments do not indicate any sequence specificity of loops during mitosis (25, 31), suggesting a major refolding of the genome that is stochastic in nature.

Chromosomes Can Be Completely Disentangled via Compacting Optimal Loops. Optimal brush chromosomes are semiflexible polymers, because the thermal persistence length of optimal chromosomes is comparable to its axial length. The long persistence length is a result of compaction tension along the backbone, which makes the brush stiff to bending fluctuations. This leads to a significantly lower number of statistical segments of the optimal brush than that of the constituting chromatin ($N' \ll N$), causing a lower level of entanglement between brush chromosomes (Eq. **4**).

The equilibrated-topology entanglement level $\langle \mathrm{Ca}^2 \rangle$ (Eq. **4**) may be estimated as proportional to the number of interchromosomal contacts per chromosome; each contact represents a point where a crossing between 2 genomic segments can be reversed in sign without significant perturbation of chromosome conformation (7). Unfolded chromosomes generally show a high degree of interchromosomal entanglement (Fig. 3*A*), since the scale of nuclear confinement is smaller than the unperturbed equilibrium random-coil size of unlooped chromosomes (Eq. **1**) (1).

Higher confinement volume upon nuclear envelope breakdown (NEB) is a mild effect and by itself does not strongly drive segregation of chromosomes (Fig. 3a). Interestingly, nematodes and yeast have essentially disentangled genomes even in a random-coil state, indicating that segregation of chromosomes is a less pressing concern for these organisms compared to, e.g., mammals, whose chromosomes can get highly entangled. Some lower eukarya (e.g., budding yeast) are known to not have NEB during mitosis, i.e., "closed" mitosis (46); the essentially disentangled genome inside the nucleus of these organisms may have contributed to this evolutionary outcome.

The entanglement level is much lower (for given confinement volume fraction and chromosome size) when the chromosomes are organized as a tandem array of optimal loops (Fig. 3*B*), highlighting the importance of loops during interphase. Fig. 3*B* is plotted for $m = 10^3$, a regime in which the optimal brush is

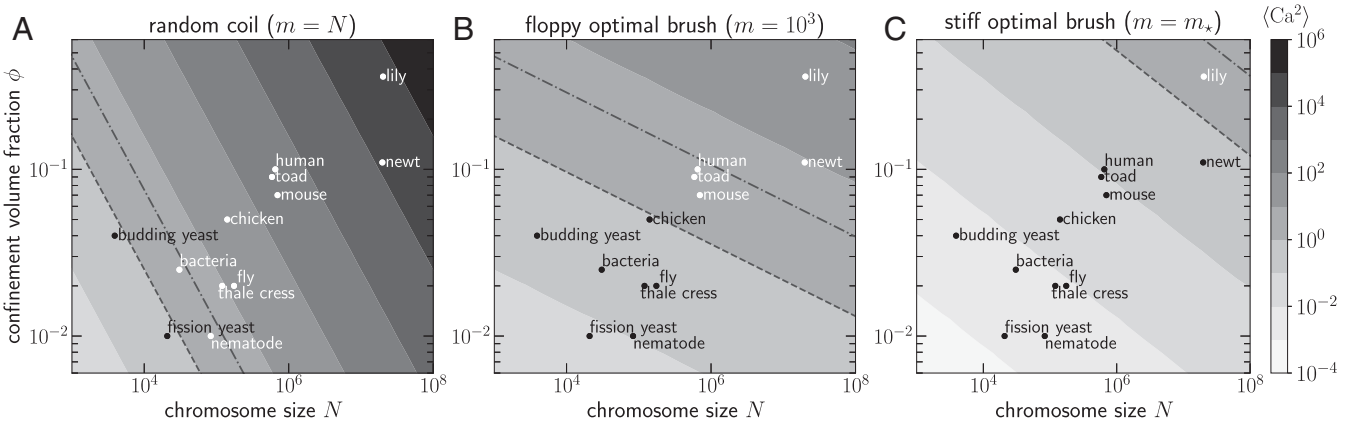

Fig. 3. Removal of interchromosomal entanglements by establishing an optimal brush configuration via loop extrusion in the presence of topology fluctuations. A cell with a given nucleus volume, number of chromosomes, and an average chromosome size *N* occupies a specific position in the (*N*, ϕ) diagram, where ϕ is the net volume fraction of all of the chromosomes within nuclear confinement. Shading indicates level of entanglement $\langle \mathrm{Ca}^2 \rangle$ (Eq. **4**), where a lighter (darker) shade depicts a lower (higher) entanglement or interchromosomal contacts per chromosome (key to *Right*). Dashed line shows $\langle \mathrm{Ca}^2 \rangle = 1$ in the nucleus: Above this line cellular chromosomes are entangled ($\langle \mathrm{Ca}^2 \rangle > 1$), while a cell lying below the dashed line has a disentangled genome ($\langle \mathrm{Ca}^2 \rangle < 1$). Dotted-dashed line shows the $\langle \mathrm{Ca}^2 \rangle = 1$ line after NEB, where the confinement volume is increased 3-fold over that of the nucleus; NEB mildly aids chromosome disentanglement. (*A*) Chromosomes considered as random coils of self-avoiding polymers exhibit a significant degree of entanglement ($\langle \mathrm{Ca}^2 \rangle_0 \sim N\phi^{5/4}$) that increases with the chromosome size. Notably, yeast chromosomes are essentially disentangled in the random-coil state. (*B* and *C*) Chromosomes modeled as polymer brushes are more compact and as a result are less entangled. Entanglements between chromosomes can be reduced by organizing the chromosomes into a tandem array of optimal loops, which have a minimal end-to-end extension for a given backbone segment size *m*. Contour plots show that steady-state optimal brush chromosomes have a lower entanglement level than the random-coil state. Further removal of entanglements is possible by stiffening the optimal brush via stretching and shortening the backbone. Interphase chromosomes have larger loops separated by long backbone segments, making them less compact, floppy brushes that are also less entangled than a random coil. The loop-extrusion mechanism can modulate the brush configuration to generate an order $k_BT/a \approx 0.4$-pN tension that completely stretches the backbone ($m = m_\star$), ultimately leading to stiffening and complete disentanglement of chromosomes.

relatively "floppy"; i.e., the backbone size is such that adjacent loops moderately overlap ($m_\star < m < n_\star$). While a smaller backbone size ($m = m_\star$, Fig. 3*C*) corresponds to a stiffer and shorter brush.

Fig. 3*A* shows the maximum possible entanglement between chromosomes for a given confinement volume fraction and average (linear) chromosome size: Due to interphase looping, chromosomes are never strongly entangled. Reducing backbone size (lower m) further lowers the level of interchromosomal entanglements (Fig. 3*C*). Stretching and shortening the backbone lead to a stiffening response of the optimal brush that drives the disentangled state. Given typical nuclear volume fractions, stretching the backbone of optimal brush chromosomes (force ≈ 1 pN) completely disentangles them.

Compact Chromosomes Have a Dense Axial Core Featuring Closely Packed Monomers That Impart Mechanical Rigidity. Compaction of the optimal brush chromosomes can be controlled via 2 physical processes: 1) shortening the backbone (lower m) and 2) increasing the valency of the optimal loops (higher α). Both these processes increase the monomer concentration in the interior of the brush, leading to an overall compaction; however, the signatures of these processes on the compacted structure are different: Shortening the backbone compacts the axial length (Eq. **2**), while increasing the average valency of optimal loops compacts the lateral dimension or thickness of the chromosomes: $R \sim \alpha^{-1/2}$.

Higher monomer concentration inside the brush leads to a densely packed core where the monomer volume fraction is near maximal ($\approx$1), and consequently, the core has a high osmotic pressure $\approx k_B T/a^3 \approx 4$ kPa. This contrasts with the much smaller bulk modulus for an ordinary (uncross-linked) semidilute polymer solution $\approx$10 Pa, due to a lower volume fraction $\approx$0.1. The elastic modulus of brush chromosomes shows a strong dependence on the average loop valency: $E \sim \alpha^{9/4}$. We use the experimental value of metaphase chromosome elastic modulus $E_{\rm meta} \approx 1$ kPa (45, 47, 48) to determine the metaphase loop valency for an optimal brush with fully stretched backbone: $\alpha_\star \approx cN^{40/89}$. Here $c = (E_{\rm meta} a^3/k_B T)^{4/9} \approx 0.5$ is an order-unity constant (Table 1).

Fig. 4 *A*–*C* shows the structural aspects of the brush chromosomes for various m and α, where the key is identical to that in Fig. 2. The axial contour length in our model does not depend on loop subdivision, so Fig. 4*A* shows only 2 curves corresponding to different values of m. This indicates that there is not a large decrease in axial contour length during the later (prometaphase) stages of mitotic compaction where loops are subdivided (α

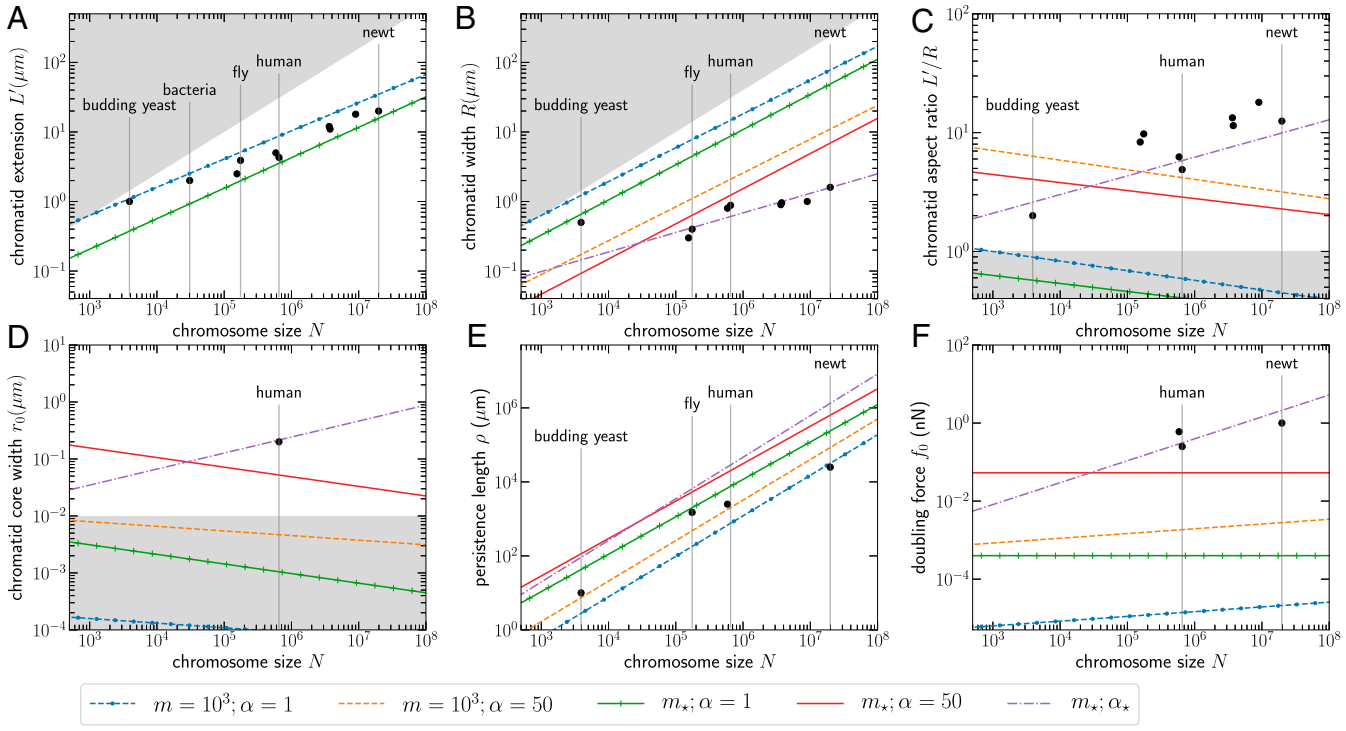

Fig. 4. Structure and mechanics of compact mitotic chromosomes result from the densely packed chromatin core. Solid circles show experimental values for metaphase chromosomes (*SI Appendix*). For the bacterial case, the solid circle shows the dimension of a cellular chromosome which compares with the cellular dimensions. Lines correspond to the cases described for Fig. 2. (*A*–*C*) Average chromatid axial length L' (*A*), chromatid width R (*B*), and length-to-width aspect ratio (L'/R) (*C*) show that the change in width is stronger upon stiffening the brush via shortening the backbone (lower m) and increasing the loop valency (higher α). Larger valency values promote a higher monomer concentration in the interior of the brush and generate a core where the monomers are densely packed. The core enhances the mechanical rigidity of the chromosomes; the width of the core r_0, which is proportional to the average loop valency, is plotted in *D*; the lines lying in the shaded region in *D* do not have a core, since a minimal core must be at least one monomer thick. The experimental data for the human chromosome core correspond to the thickness of the axial region where condensins colocalize in metaphase (23). The thermal persistence length of the brush ρ (*E*) and the force associated with stretching the chromosome to twice its native length or the doubling force f_0 (*F*) show increased stiffness and mechanical rigidity for smaller backbone and higher valency. The valency $\alpha_\star$, which is required to reproduce the observed metaphase chromosome elastic modulus $\approx$1 kPa and is $\approx$40% of the maximum allowed valency of an optimal loop, agrees well with metaphase chromosome size data. This indicates that the dense core resulting from backbone stretching and branching of chromosomal loops, achievable via a loop extrusion mechanism, can underlie the emergent mechanical rigidity and compactness of metaphase chromosomes. The shaded region in *A* and *B* corresponds to the chromosome for which the backbone is comparable to the loop size leading to no overlap between adjacent loops, which approaches the random-coil limit of the polymer brush: $L' \approx R_F(N)$ and $R \approx R_F(N)$. This suggests bacterial chromosomes are only minimally compacted in the axial dimension. Also, note that backbone segments with $m = 1{,}000$ monomers correspond to overlapping adjacent optimal loops for all relevant chromosome sizes.

increased) (25). The thickness, however, undergoes significant compaction upon subdivision of loops (Fig. 4*B*).

Comparison with metaphase data suggests that metaphase chromosomes have a sufficiently stretched backbone ($m = m_\star$) supporting highly branched loops ($\alpha \gg 1$). The core for metaphase chromosomes of higher eukarya is expected to be $\approx$100 nm thick (Fig. 4*D*). The thermal bending persistence length and the doubling force (force required to stretch a chromosome to twice its native length: an intensive quantity) are measures of mechanical rigidity and show strengthening of the brush in metaphase due to formation of the thick core (Fig. 4 *E* and *F*) (*SI Appendix*). Metaphase doubling force originates primarily from the core; however, this force is not equivalent to the polymer backbone stretching force that increases interloop distance d. This force is a product of the high osmotic pressure generated in the core from dense packing, which possibly depends heavily on chromatin cross-linking. Additionally, local adhesion among the core monomers may also provide stabilization.

Bacterial Chromosomes. Bacteria, unlike eukaryotes, do not have nucleosomes; instead, bacterial DNA inside cells is coated with a variety of NAPs, e.g., HU, H-NS, and IHF (49). Like eukaryotes, bacteria possess SMC proteins [in *Escherichia coli*, MukBEF (50)] and bacterial versions of eukaryote Topo II. We treat bacterial chromosomes as self-avoiding polymers, with cylindrical monomer units of length $a \approx 50$ nm [comparable to the persistence length of naked DNA (51)] and width $b \approx 5$ nm, corresponding to the thickness of protein-bound DNA segments (NAPs can reduce the persistence length but this is not crucial here). This gives a monomer aspect ratio constant $a/b \approx 10$ that shows up in the ratio between volume and excluded volume of a monomer. The macroscopic (renormalized) lengths, L' and R, scale weakly with the aspect ratio (*SI Appendix*), making the structure optimization and entanglement discussions for spherical monomers applicable to bacterial chromosomes.

The bacterial genome has the potential to be appreciably entangled due to its substantial confinement (Fig. 3*A*), highlighting the need to drive compaction to segregate multiple copies. However, only mild compaction compared to that in higher eukaryotes is required (Fig. 3*B*). Bacterial DNA is also subject to a global supercoiling pressure, by virtue of DNA gyrase, a motor-like enzyme that maintains bacterial DNA in a supercoiled condition. Supercoiling may play an important role in driving compaction and maintaining an optimal brush conformation of bacterial chromosomes. The restoring force of a plectonemic domain for physiological levels of bacterial supercoiling $\approx$0.5 pN (52) can generate the stretching tension along the backbone connecting plectonemic domains, necessary to drive compaction and segregation of bacterial chromosomes. This is in accord with models of bacterial chromosome organization into territories driven by DNA supercoiling (53).

For elongated bacterial cells that are asymmetric (e.g., *E. coli* and *Caulobacter crescentus*), there is expected to be an entropic-segregation pressure gradient along the long axis of the cell. This may aid chromosome segregation by pushing the 2 sister chromosomes to opposite poles of the long axis (54). The cylindrical brush structure of chromosomes, driven by loop extrusion, enhances this pressure gradient and provides an active mechanism to control segregation. Other mechanisms may work in parallel: Some bacterial species possess chromosome tethering mechanisms that may aid in driving axial segregation (55).

The optimal loop result for the *E. coli* nucleoid of axial length 2 μm corresponds to a floppy brush (blue dashed line in Fig. 4*A*), which permits full segregation but with enough flexibility to allow the nucleoid to be folded and moved around inside the cell. The bacterial nucleoid is heavily confined, evident from the large expansion (3- to 10-fold linear dimension) of the bacterial chromosome following cell lysis. Bacterial nucleoids removed from cells behave as polymer networks of roughly 10- to 20-μm maximum extension, (55, 56), consistent with the maximum extension of a loosely compacted brush of axial length ≈ 2 μm.

Discussion

We used a polymer model to describe cellular chromosomes in confinement and showed that a chromosome structure characterized by an array of connected chromatin/DNA loops, in the presence of topology fluctuations via random strand passage by Topo II, exhibits lower interchromosomal entanglement than the corresponding unfolded, linear-polymer configuration. We found that folding a chromosome in loops of a chromosome-size–dependent length—the "optimal" loop length—simultaneously maximizes compaction and minimizes interchromosomal entanglements (Figs. 2 and 3).

These optimal loops (or subloops formed upon branching) are comparable to experimentally observed loops through the cell cycle, suggesting a role of chromosomal loops in suppressing entanglements, during both interphase and mitosis. These loops keep the chromosomes territorialized throughout the cell cycle, tightly regulating interchromosome entanglement. Larger loops and a longer backbone allow a controlled level of entanglement in interphase, which is likely essential for gene expression. While the positioning of these loops may affect transcriptional regulation, correspondence of their sizes to that of entanglement-suppressing optimal loops may be linked with the evolutionary selection of chromosome architecture.

On the other hand, compact mitotic chromosomes have short, stretched backbones with heavily branched loops that efficiently remove all of the entanglements between chromosomes, leading to their segregation (Fig. 3). Mitotic chromosomes have a densely packed core along their cylindrical axes. The high density of monomers in the core is responsible for the emergent mechanical stiffness of chromosomes during mitosis. The predicted size of mitotic subloops required to reproduce the experimentally observed chromosome stiffness is smaller than that of the subloops observed in electron-microscope images (Fig. 2). A larger subloop in our model will lead to lower chromosome stiffness moduli; however, the mechanical rigidity may be compensated by additional cross-linking of chromatin inside the chromosome brush, which we ignore in our simple approach.

Topo II-driven topology fluctuations maintain a steady-state topology essential for segregation and disentanglement via compaction. Topo IIs allow passage of chromatin segments through one another, permitting chromosome topology to fluctuate (2). However, Topo IIs cannot disentangle chromosomes by themselves (57–60), since they are unable to directly sense global chromosome topology. By allowing topology fluctuations, Topo II can maintain topological equilibrium, allowing disentanglement to occur gradually as lengthwise compaction proceeds. Our theory shows that the entanglement level tracks the chromosome architecture and its manipulation by loop extrusion (see below). Further work on the time evolution of entanglement release is a next step: DNA tension at interlocks and effective viscosity generated by entanglements are likely to be important.

We have assumed the null hypothesis of random strand passage by Topo II; a synergistic mechanism where Topo II directly interacts with SMC complexes has been suggested to drive more efficient disentanglement (5). Intrachromosomal topology, such as chromatin knots, has also been shown to be suppressed by a combined action of SMC and Topo II (4). In our model, loop-extrusion folding of chromatin by SMCs provides a local free-energy gradient pushing Topo II to resolve interchromosome

catenation, thus also coupling SMC activity to topology changes mediated by Topo II.

Loop Extrusion Can Control the Optimal Brush Structure. Loop extrusion has emerged as a vital mechanism underlying organization of chromosomes. SMC complexes (cohesin and condensins) can exert piconewton forces and are the prime candidates for driving the loop extrusion activity (26, 27, 61–64). In our model, extrusion of loops generates interloop repulsion that stretches the backbone; thus, loop extrusion may effectively control n, m, and α to drive chromosome compaction and, consequently, disentanglement in the presence of Topo II. The ubiquitous presence of DNA-bound SMC complexes in all cells can ensure a steady-state stretching of backbone segments, important for maintaining a semiflexible chromosome brush, and a low entanglement level between confined chromosomes throughout the cell cycle.

The Rouse equilibration time of a typical optimal loop (100 to 1,000 monomers) is less than 1 s, with topology changes requiring roughly 1 s per strand passage cycle. The relevant timescale associated with loop extrusion activity is not clear; individual SMC motors have been observed to translocate on DNA at $\sim$ 1 kb/s (27). However, any large-scale structural reorganization involving megabase-pair–sized chromosome loops is expected to occur over at least many minutes (i.e., in mammals, on the order of 10 traversals of $\approx$100-kb loops of chromatin by SMCs moving at kilobase per second speeds, or roughly $\approx 10^3$ s, similar to the duration of mammalian prophase), much longer than the Rouse time of the loops. This allows us to use static scaling laws that are governed by the elasticity of chromatin. Analysis of the dynamics during the reorganization process may be possible by combining relaxational polymer dynamics, topology change by Topo II, and estimates of nonequilibrium active forces generated by SMC complexes.

Chromosome Loop Organization during Interphase. The size of the interphase loops and their positioning depend on proper functioning of the loop-extruding SMC complexes. Destabilization of interphase loops (possibly via inhibition of SMC activity) is expected to disrupt the optimal structure, resulting in higher chromosomal overlap, i.e., weakening of chromosomal territories, as has been observed (22). We also expect a concomitant increase in the interchromosomal entanglements for less territorial chromosomes.

Compartmentalization of the genome into early- and late-replicating domains (respectively, eu- and heterochromatin) may be relevant to maintaining low genome entanglement during DNA replication. Replication is expected to cause disassembly of loops, especially when replicating the loop anchoring regions, likely leading to an overall increase in entanglement between chromosomes. A controlled disassembly of loop organization via compartmental replication (and possibly restoration of loops immediately following replication) restricts large-scale entropic mixing of chromosomes during S phase.

Various non-SMC complexes, such as CTCF proteins, are integral to chromosome architecture and are possibly relevant for the optimal structure. CTCF proteins are known to stabilize certain sequence-specific loops that play a role in gene regulation (32), and some of these loops have also been reported to remain stably bound throughout the cell cycle (65, 66). Such a structural template of connected loops is capable of storing heritable gene expression patterns while simultaneously minimizing chromosomal entanglements.

DNA twisting or supercoiling pressure is another important aspect of chromatin, especially during interphase, when the DNA is transcribed and replicated. Supercoiling flux, e.g., at the loop anchors, may regulate the level of loop compaction and stabilize certain loops (53).

Chromosome Structural Rigidity and Topological Disentanglement during Mitosis. Loop extrusion activity by SMC complexes maximizes compaction by minimizing the axial length of brush chromosomes. Condensin II is a likely candidate that drives the prophase compaction, suggesting an important role of condensin II in determining the axial length of chromosomes, in accord with the observation of an increase in the axial length for condensin II-depleted chromosomes (17, 23, 67–69). Note that due to the optimal loop architecture of chromosomes in interphase, we do not expect the axial length to significantly change during the course of the cell cycle—which is central to our conclusion that interchromosomal entanglements are suppressed by SMC activity during the cell cycle.

The other SMC complex, cohesin, is known to hold the sister chromatids during mitosis; however, its role in prophase compaction of chromosomes, if any, is not clear. If indeed condensin II is solely driving prophase compaction and segregation, inactivation of cohesin activity in prophase will lead to a factor-of-2 increase in the number of chromosomes, which is not predicted to be crucially detrimental to their segregation (Fig. 3*C*).

The radial dimension of cylindrical chromosomes is strongly compacted by loop division, which establishes a dense core along the axes (Fig. 4). Higher valencies corresponding to branched loops in metaphase may occur for eukaryote chromosomes via binding of condensin I after nuclear envelope breakdown (25). The observation that condensin I-depleted chromosomes have a thicker diameter and a lower stiffness (17, 68, 70) supports the notion that these proteins branch loops established by condensin II during prophase, to generate rigid, rod-like metaphase chromosomes.

SMC activity is crucial for the dense core in metaphase chromosomes. The high osmotic pressure from close packing of nucleosomes in the core is possibly stabilized by additional mechanisms such as nucleosome–nucleosome attraction in mitosis (71) and a higher concentration of chromatin cross-linking proteins (including Topo II) inside the axial core. A recent proposal, supported by Hi-C studies, posits that SMC complexes drive a helical brush axis during metaphase (25). Such phenomenology may be studied within the framework of our model, which is left for future discourse.

Segregation of Sister Chromatids from Osmotic Repulsion between the Axial Cores. Loop-extrusion activity on the newly replicated catenated sister chromosomes leads to 2 brushes that are intertwined near their backbones; the overlapping loops generate a repulsive interchromatid force. The net repulsive force follows from the total osmotic pressure per cross-sectional area of overlap between the 2 sister chromatids, giving a force acting on each loop of $f_{rep} \approx 10$ pN for monovalent loops, and increases strongly for higher loop valencies $f_{rep} \sim \alpha^{1/2}$ (*SI Appendix*). This repulsion drives strand passages by Topo II that will lead to physical segregation of sister-chromosome brushes.

Importantly, an indiscriminate increase of loop valency and cross-linking while the sister-chromatid backbones are still heavily entangled will lead to fusion of the sister chromosomes into a common core, hindering their segregation. This predicts heavily entangled sister chromosomes if condensin I is active inside the nucleus during prophase. Initiation of condensin II compaction and sister-chromosome segregation immediately following replication (72, 73) are crucial for timely removal of entanglements before establishing a thick core (i.e., before condensin I activity). Once the backbones are disentangled, removal of residual entanglements between sister-chromatid loops is facilitated by core formation, since the repulsive force between chromatid backbones is higher for a thicker core. Our model rationalizes the sharp, disjoint compartmentalization of condensin II and condensin I in terms of a kinetic process: Establish packed loop arrays first (condensin II) and then generate a dense core by loop

valency increase (condensin I), which is in line with conclusions drawn from Hi-C analyses (25).

Fusion of the sister-chromatid cores near the centromeric region is unavoidable (the sisters remain attached there until anaphase). High concentrations of Topo IIs and SMCs at the centromere during metaphase, resulting from the high DNA density, will generate strong repulsive forces between the dense and short centromeric loops, possibly playing a crucial role in disentanglement of the (peri)centromeric regions (74, 75).

The smallest length scale in our analysis is the nucleosome/monomer size ($\approx$10 nm), so we do not explicitly consider effects of electrostatic interactions which are of shorter range (the screening length is $\approx$1 nm under the 0.15-M univalent salt conditions found in the nucleus). Of course, local interactions generated by electrostatic interactions, especially due to divalent or multivalent charged species, play a key role in chromosome organization, e.g., local adhesion between nucleosomes or DNA site-specific interactions, but for this paper we are concerned with larger-scale chromosome organization.

In conclusion, we have developed a steady-state polymer brush model for chromosomes, where the brush structure is primarily controlled via loop extrusion. Our major result is that the loop organization of the cellular genome is an entanglement-suppressing structure, explaining experimental observations. Lengthwise compaction of the brush results in chromosome segregation, establishing that loop extruders are capable of driving chromosome individualization and chromatid segregation.

ACKNOWLEDGMENTS. We acknowledge funding from NIH Grants R01-GM105847, U54-CA193419 (CR-PS-OC), and U54-DK107980 (4DNucleome). S.B. acknowledges funding from the Welch Foundation (Grant C-1792). We thank E. Banigan, A. D. Stephens, R. Biggs, and the reviewers for their helpful discussions.

1. P. G. DeGennes, *Scaling Concepts in Physics* (Cornell University, Ithaca, NY, 1977).
2. J. L. Sikorav, G. Jannink, Kinetics of chromosome condensation in the presence of topoisomerases: A phantom chain model. *Biophys. J.* **66**, 827–837 (1994).
3. A. Goloborodko, J. F. Marko, L. A. Mirny, Chromosome compaction by active loop extrusion. *Biophys. J.* **110**, 2162–2168 (2016).
4. D. Racko, F. Benedetti, D. Goundaroulis, A. Stasiak, Chromatin loop extrusion and chromatin unknotting. *Polymers (Basel)* **10**, 1126 (2018).
5. E. Orlandini, D. Marenduzzo, D. Michieletto, Synergy of topoisomerase and structural-maintenance-of-chromosomes proteins creates a universal pathway to simplify genome topology. *Proc. Natl. Acad. Sci. U.S.A.* **116**, 8149–8154 (2019).
6. J. F. Marko, Linking topology of tethered polymer rings with applications to chromosome segregation and estimation of the knotting length. *Phys. Rev. E* **79**, 051905 (2009).
7. J. F. Marko, Scaling of linking and writhing numbers for spherically confined and topologically equilibrated flexible polymers. *J. Stat. Phys.* **142**, 1353–1370 (2011).
8. E. Alipour, J. F. Marko, Self-organization of domain structures by DNA-loop-extruding enzymes. *Nucleic Acids Res.* **40**, 11202–11212 (2012).
9. J. R. Paulson, U. K. Laemmli, The structure of histone-depleted metaphase chromosomes. *Cell* **12**, 817–828 (1977).
10. M. P. F. Marsden, U. K. Laemmli, Metaphase chromosome structure: Evidence for a radial loop model. *Cell* **17**, 849–858 (1979).
11. J. B. Rattner, C. C. Lin, Radial loops and helical coils coexist in metaphase chromosomes. *Cell* **42**, 291–296 (1985).
12. D. Racko, F. Benedetti, J. Dorier, A. Stasiak, Transcription-induced supercoiling as the driving force of chromatin loop extrusion during formation of TADs in interphase chromosomes. *Nucleic Acids Res.* **46**, 1648–1660 (2017).
13. C. A. Brackley *et al.*, Nonequilibrium chromosome looping via molecular slip links. *Phys. Rev. Lett.* **119**, 138101 (2017).
14. C. A. Miermans, C. P. Broedersz, Bacterial chromosome organization by collective dynamics of SMC condensins. *J. R. Soc. Interface* **15**, 20180495 (2018).
15. B. Zhang, P. G. Wolynes, Shape transitions and chiral symmetry breaking in the energy landscape of the mitotic chromosome. *Phys. Rev. Lett.* **116**, 248101 (2016).
16. M. Di Pierro, B. Zhang, E. L. Aiden, P. G. Wolynes, J. N. Onuchic, Transferable model for chromosome architecture. *Proc. Natl. Acad. Sci. U.S.A.* **113**, 12168–12173 (2016).
17. T. Ono *et al.*, Differential contributions of condensin I and condensin II to mitotic chromosome architecture in vertebrate cells. *Cell* **115**, 109–121 (2003).
18. T. Hirota, D. Gerlich, B. Koch, J. Ellenberg, J.-M. Peters, Distinct functions of condensin I and II in mitotic chromosome assembly. *J. Cell Sci.* **117**, 6435–6445 (2004).
19. M. Sun, R. Kawamura, J. F. Marko, Micromechanics of human mitotic chromosomes. *Phys. Biol.* **8**, 1–18 (2011).
20. G. Wutz *et al.*, Topologically associating domains and chromatin loops depend on cohesin and are regulated by CTCF, WAPL, and PDS 5 proteins. *EMBO J.* **36**, 3573–3599 (2017).
21. T. Ono, C. Sakamoto, M. Nakao, N. Saitoh, T. Hirano, Condensin II plays an essential role in reversible assembly of mitotic chromosomes in situ. *Mol. Biol. Cell* **28**, 2875–2886 (2017).
22. L. F. Rosin, S. C. Nguyen, E. F. Joyce, Condensin II drives large-scale folding and spatial partitioning of interphase chromosomes in Drosophila nuclei. *PLoS Genet.* **14**, 1–26 (2018).
23. N. Walther *et al.*, A quantitative map of human condensins provides new insights into mitotic chromosome architecture. *J. Cell Biol.* **217**, 2309–2328 (2018).
24. L. Vian *et al.*, The energetics and physiological impact of cohesin extrusion. *Cell* **173**, 1165–1178.e20 (2018).
25. J. H. Gibcus *et al.*, A pathway for mitotic chromosome formation. *Science* **359**, eaao6135 (2018).
26. T. Terakawa *et al.*, The condensin complex is a mechanochemical motor that translocates along DNA. *Science* **358**, 672–676 (2017).
27. A. M. Ganji *et al.*, Real-time imaging of DNA loop extrusion by condensin. *Science* **360**, 102–105 (2018).
28. E. Lieberman-Aiden *et al.*, Comprehensive mapping of long-range interactions reveals folding principles of the human genome. *Science* **326**, 289–293 (2009).
29. E. P. Nora *et al.*, Spatial partitioning of the regulatory landscape of the X-inactivation center. *Nature* **485**, 381–385 (2012).
30. T. Sexton *et al.*, Three-dimensional folding and functional organization principles of the Drosophila genome. *Cell* **148**, 458–472 (2012).
31. N. Naumova *et al.*, Organization of the mitotic chromosome. *Science* **342**, 948–953 (2014).
32. S. S. P. Rao *et al.*, A 3D map of the human genome at kilobase resolution reveals principles of chromatin looping. *Cell* **159**, 1665–1680 (2014).
33. A. L. Sanborn *et al.*, Chromatin extrusion explains key features of loop and domain formation in wild-type and engineered genomes. *Proc. Natl. Acad. Sci. U.S.A.* **112**, E6456–E6465 (2015).
34. J. F. Marko, E. D. Siggia, Polymer models of meiotic and mitotic chromosomes. *Mol. Biol. Cell* **8**, 22217–22231 (1997).
35. Y. Nishino *et al.*, Human mitotic chromosomes consist predominantly of irregularly folded nucleosome fibres without a 30-nm chromatin structure. *EMBO J.* **31**, 1644–1653 (2012).
36. K. Maeshima, S. Ide, M. Babokhov, Dynamic chromatin organization without the 30-nm fiber. *Curr. Opin. Struct. Biol.* **58**, 95–104 (2019).
37. H. D. Ou *et al.*, ChromEMT: Visualizing 3D chromatin structure and compaction in interphase and mitotic cells. *Science* **357**, eaag0025 (2017).
38. A. Lesage, V. Dahirel, J. M. Victor, M. Barbi, Polymer coil-globule phase transition is a universal folding principle of Drosophila epigenetic domains. *Epigenet. Chromatin* **12**, 28 (2019).
39. S. Panyukov *et al.*, Tension amplification in molecular brushes in solutions and on substrates. *J. Phys. Chem. B* **113**, 3750–3768 (2009).
40. H. Li, T. A. Witten, Polymers grafted to convex surfaces: A variational approach. *Macromolecules* **27**, 449–457 (1994).
41. L. Feuz, F. A. M. Leermakers, M. Textor, O. Borisov, Bending rigidity and induced persistence length of molecular bottle brushes: A self-consistent-field theory. *Macromolecules* **38**, 8891–8901 (2005).
42. M. Daoud, J. P. Cotton, Star shaped polymers: A model for the conformation and its concentration dependence. *J. Phys.* **43**, 531–538 (1982).
43. A. Rosa, R. Everaers, Structure and dynamics of interphase chromosomes. *PLoS Comp. Biol.* **4**, e1000153 (2008).
44. D. W. Schaefer, J. F. Joanny, P. Pincus, Dynamics of semiflexible polymers in solution. *Macromolecules* **13**, 1280–1289 (1980).
45. J. F. Marko, Micromechanical studies of mitotic chromosomes. *Chromosome Res.* **16**, 469–497 (2008).
46. S. Sazer, M. Lynch, D. Needleman, Deciphering the evolutionary history of open and closed mitosis. *Curr. Biol.* **24**, R1099–R1103 (2014).
47. B. Houchmandzadeh, J. F. Marko, D. Chatenay, A. Libchaber, Elasticity and structure of eukaryote chromosomes studied by micromanipulation and micropipette aspiration. *J. Cell Biol.* **139**, 1–12 (1997).
48. M. G. Poirier, S. Eroglu, J. F. Marko, The bending rigidity of mitotic chromosomes. *Mol. Biol. Cell* **13**, 2170–2179 (2002).
49. K. K. Swinger, P. A. Rice, IHF and HU: Flexible architects of bent DNA. *Curr. Opin. Struct. Biol.* **14**, 28–35 (2004).
50. V. V. Rybenkov, V. Herrera, Z. M. Petrushenko, H. Zhao, MukBEF, a chromosomal organizer. *J. Mol. Microbiol. Biotechnol.* **24**, 371–383 (2014).
51. J. F. Marko, E. D. Siggia, Stretching DNA. *Macromolecules* **28**, 8759–8770 (1995).
52. J. F. Marko, Torque and dynamics of linking number relaxation in stretched supercoiled dna. *Phys. Rev. E* **76**, 021926 (2007).
53. F. Benedetti, J. Dorier, Y. Burnier, A. Stasiak, Models that include supercoiling of topological domains reproduce several known features of interphase chromosomes. *Nucleic Acids Res.* **42**, 2848–2855 (2014).
54. S. Jun, B. Mulder, Entropy-driven spatial organization of highly confined polymers: Lessons for the bacterial chromosome. *Proc. Natl. Acad. Sci. U.S.A.* **103**, 12388–12393 (2006).
55. X. Wang, P. M. Llopis, D. Z. Rudner, Organization and segregation of bacterial chromosomes. *Nat. Rev. Genet.* **14**, 191–203 (2013).
56. J. Pelletier *et al.*, Physical manipulation of the *Escherichia coli* chromosome reveals its soft nature. *Proc. Natl. Acad. Sci. U.S.A.* **109**, E2649–E2656 (2012).

57. O. Cuvier, T. Hirano, A role of topoisomerase II in linking DNA replication to chromosome condensation. *J. Cell Biol.* **160**, 645–655 (2003).
58. P. A. Coelho, Condensin-dependent localisation of topoisomerase II to an axial chromosomal structure is required for sister chromatid resolution during mitosis. *J. Cell Sci.* **116**, 4763–4776 (2003).
59. E. Piskadlo, A. Tavares, R. A. Oliveira, Metaphase chromosome structure is dynamically maintained by condensin I-directed DNA (de)catenation. *eLife* **6**, e26120 (2017).
60. M. Sun, R. Biggs, J. Hornick, J. F. Marko (2018) Condensin controls mitotic chromosome stiffness and stability without forming a structurally contiguous scaffold. *Chromosome Res.* **26**, 277–295.
61. M. Sun, T. Nishino, J. F. Marko, The SMC1-SMC3 cohesin heterodimer structures DNA through supercoiling-dependent loop formation. *Nucleic Acids Res.* **41**, 6149–6160 (2013).
62. R. A. Keenholtz *et al.*, Oligomerization and ATP stimulate condensin-mediated DNA compaction. *Sci. Rep.* **7**, 14279 (2017).
63. J. M. Eeftens, S. Bisht, J. Kerssemakers, M. Kschonsak, C. H. Haering, Real-time detection of condensin-driven DNA compaction reveals a multistep binding mechanism. *EMBO J.* **36**, 3448–3457 (2017).
64. J. F. Marko, P. D. L. Rios, A. Barducci, S. Gruber, DNA-segment-capture model for loop extrusion by structural maintenance of chromosome (SMC) protein complexes. *Nucleic Acids Res.* **47**, 6956–6972 (2019).
65. L. J. Burke *et al.*, CTCF binding and higher order chromatin structure of the H19 locus are maintained in mitotic chromatin. *EMBO J.* **24**, 3291–3300 (2005).
66. W. Shen *et al.*, A possible role of Drosophila CTCF in mitotic bookmarking and maintaining chromatin domains during the cell cycle. *Biol. Res.* **48**, 27 (2015).
67. K. Shintomi, T. Hirano, The relative ratio of condensin I to II determines chromosome shapes. *Gen. Dev.* **25**, 1464–1469 (2011).
68. L. C. Green *et al.*, Contrasting roles of condensin I and condensin II in mitotic chromosome formation. *J. Cell Sci.* **125**, 1591–1604 (2012).
69. M. Houlard, J. Godwin, J. Metson, J. Lee, T. Hirano, Condensin confers the longitudinal rigidity of chromosomes. *Nat. Cell Biol.* **17**, 771–781 (2017).
70. D. Gerlich, T. Hirota, B. Koch, J.-M. Peters, J. Ellenberg, Condensin I stabilizes chromosomes mechanically through a dynamic interaction in live cells. *Curr. Biol.* **16**, 333–344.
71. A. Zhiteneva *et al.*, Mitotic post-translational modifications of histones promote chromatin compaction in vitro. *Open Biol.* **7**, 170076 (2017).
72. C. R. Bauer, T. A. Hartl, G. Bosco, Condensin II promotes the formation of chromosome territories by inducing axial compaction of polyploid interphase chromosomes. *PLoS Comput. Biol.* **8**, 1–12 (2012).
73. T. Ono, D. Yamashita, T. Hirano, Condensin II initiates sister chromatid resolution during S phase. *J. Cell Biol.* **200**, 429–441 (2013).
74. J. Lawrimore *et al.*, DNA loops generate intracentromere tension in mitosis. *J. Cell Biol.* **210**, 553–564 (2015).
75. J. Lawrimore *et al.*, ChromoShake: A chromosome dynamics simulator reveals that chromatin loops stiffen centromeric chromatin. *Mol. Biol. Cell* **27**, 153–166 (2016).